Physica Medica 135 (2025) 104995

Contents lists available at ScienceDirect

Physica Medica

journal homepage: www.elsevier.com/locate/ejmp

Original paper

Simulation of digital mammographic images using GAMOS: Proof of concept

F.R. Lozano [a,*], V. Sanchez-Lara [a], C. Huerga [b], Luis C. Martinez-Gomez [c], D. Garcia-Pinto [a]

[a] Universidad Complutense de Madrid, Madrid, 28040, Spain
[b] Hospital Universitario La Paz, Madrid, 28046, Spain
[c] Hospital Universitario 12 de Octubre, Madrid, 28041, Spain

ARTICLE INFO

Keywords:
Mammography
Geant4
Monte carlo
Breast imaging
Simulation

ABSTRACT

Purpose: To present a simulation pipeline for digital mammography based on the GAMOS framework, enabling realistic image formation and dose estimation using high-fidelity anatomical phantoms and flexible detector modeling.

Methods: A complete *in silico* model was implemented using GAMOS and GEANT4, including a Siemens Mammomat Inspiration system geometry, VICTRE voxelized breast phantoms, and two detector models: a direct conversion detector (MCD) and a virtual detector (VD). The simulation incorporated an anti-scatter grid, dose scoring tools, and a GUI for parameter adjustment. Performance metrics were calculated according to IEC 62220-1-2:2007.

Results: The simulation yielded realistic mammographic images and accurate dose estimates. The MTF, NNPS, and DQE were calculated for both detector models and compared against published values. Maximum DQE differences were approximately 20%, with comparisons performed at spatial frequencies of 0.5, 2.0 and 5.0 mm^{-1}. The $MTF_{50\%}$ was 4.25 mm^{-1} (VD) and 4.35 mm^{-1} (MCD). Anatomical noise analysis showed β values between 2.67 and 3.16, consistent with clinical data. Dose validation against AAPM TG-195 showed differences below 1.08%.

Conclusion: The proposed simulation framework is capable of producing realistic mammographic images and accurate dose calculations using an accessible interface. This tool is suitable for virtual clinical trials and system performance evaluation, and allows further extension to advanced imaging techniques such as contrast-enhanced or phase-contrast mammography. Code: https://github.com/PREDICO-Project/MIMAC

1. Introduction

Virtual Clinical Trials (VCTs) [1,2] are emerging as a key tool in medical research, providing an early-stage assessment of innovations in imaging techniques and technology prior to human clinical studies. In mammography, VCTs are particularly relevant for evaluating new methods of early breast cancer detection, while also helping to reduce both the costs and time associated with development.

A realistic VCT generally requires two core components [3]: high-fidelity digital anatomical models and a representative simulator of the imaging system. Incorporating detailed digital phantoms [4], such as those provided by VICTRE [5,6], significantly enhances realism in breast anatomy modeling. Monte Carlo simulations play a vital role in transport characterization of X-rays, dose prediction, and image formation [7–11]. Although GPU-accelerated codes like MCGPU [12,13] within VICTRE can achieve substantial speed gains [14], more complex imaging tasks — such as contrast-enhanced spectral mammography (CESM) [15] or phase-contrast imaging (PCI) [16,17] — may require greater flexibility to model advanced physical interactions.

GEANT4 [18] stands out for its broad range of interaction models and the possibility of introducing custom physics processes [19–23]. Building on GEANT4, the GAMOS framework [24] provides a modular and accessible interface that simplifies simulation setup without requiring in-depth C++ knowledge. While GAMOS was not initially designed for direct image simulation, its capacity to handle complex geometries, materials, and physics processes also makes it suitable for mammography [25]. However, generating realistic images requires accurate modeling of the detector response, including background signal reproduction and noise power spectrum (NPS) [26], since the combination of quantum noise, anatomical noise, and detector structural noise can critically influence lesion detectability [27].

This work presents a comprehensive *in silico* digital mammography model using GEANT4 within GAMOS. The approach offers a flexible

* Corresponding author.
E-mail address: frloza03@ucm.es (F.R. Lozano).

https://doi.org/10.1016/j.ejmp.2025.104995
Received 23 October 2024; Received in revised form 5 April 2025; Accepted 29 April 2025
Available online 4 June 2025

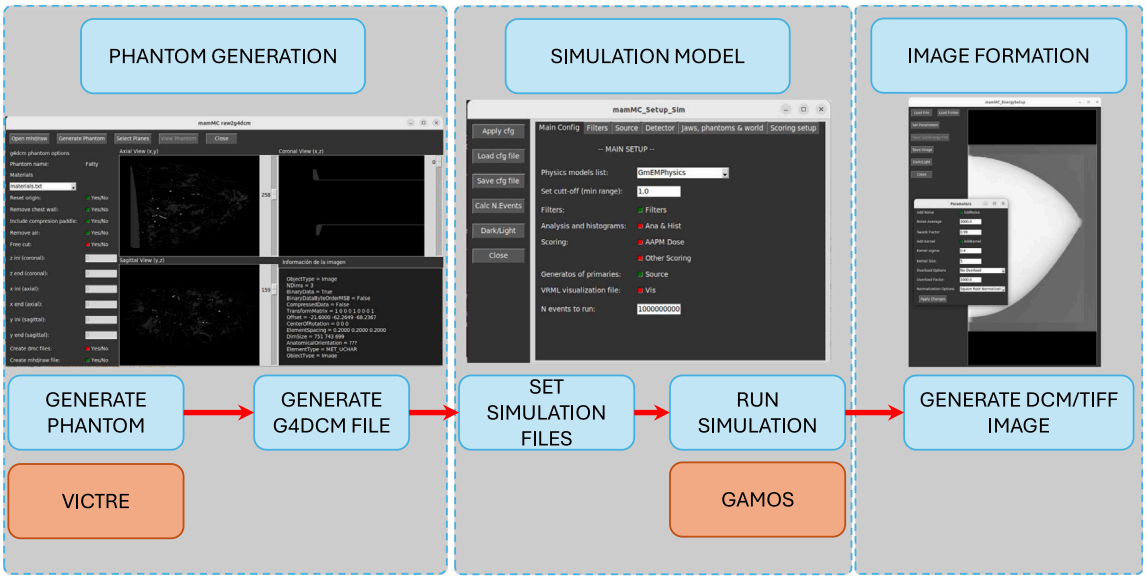

Fig. 1. Schematic illustration of the image simulation. Including details of the GUI used for parameter adjustments.

simulation pipeline for mammographic images by leveraging realistic anatomical breast models from VICTRE. It also integrates a rigorous dose-calculation method following the strategy described by Badal et al. [13], validated against established standards. This framework enables advanced performance studies of imaging systems under a range of clinical conditions and supports the investigation of new acquisition techniques or detector designs without requiring CUDA programming or extensive C++ expertise.

2. Materials and methods

We will use GAMOS interface [24] which is a toolkit that operates on GEANT4 but offers the possibility of interacting with the simulation without needing in-depth knowledge of the GEANT4 code and C++ programming language. Additionally, in the proposed simulation model, a Graphical User Interface (GUI) has been added to facilitate the adjustment of parameters.

The basic geometry of a Siemens Mammomat Inspiration system [28] was simulated to validate the proposed in silico model.

Fig. 1 illustrates the different stages in the image formation process, grouped into the following sub-processes:

- **A.- Phantom generation:** Generation of the voxelized breast phantom.
- **B.- Simulation model:** Simulation of the interaction of the beam and signal collection in the detector.
- **C.- Image formation:** Analysis of the collected signal and generation of the final image.

2.1. Phantom

Two phantoms were used for validation purposes: a geometric phantom and an anthropomorphic voxelized one. The geometric phantom is used to validate the energy deposited in the tissue. The voxelized phantom is used to obtain mammographic-like images.

The geometric phantom is based on AAPM TG-195 [29] specifications (see Fig. 2). Briefly, the setup featured a semicircular cylinder of skin 50 mm thick and 100 mm in radius, and a concentric cylinder of breast tissue 46 mm thick and 98 mm in radius. Compression paddles 2 mm thick were also included. The materials used for skin, tissue, and PMMA for paddles were defined according to the report specifications. This phantom is homogeneous and non-voxelized and is referred to as

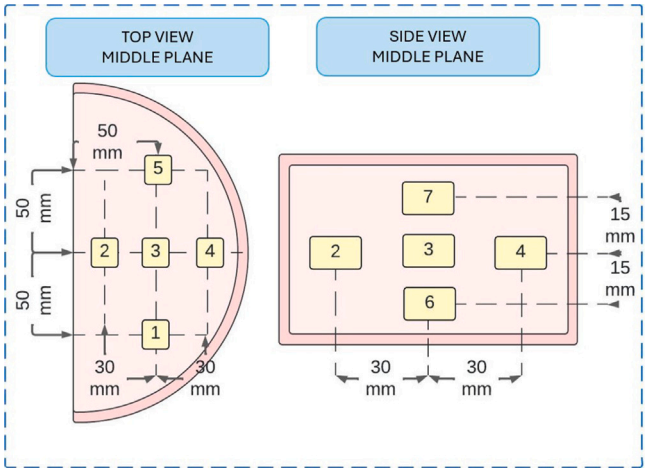

Fig. 2. AAPM TG-195 phantom diagram with the location of the VOIs.

the "AAPM phantom" to reflect its adherence to the AAPM TG-195 guidelines for dose verification.

The voxelized phantoms have been created using VICTRE (Virtual Imaging Clinical Trials for Regulatory Evaluation, [5,6]), which is capable of generating detailed breast phantoms. VICTRE allows to generate a vast number of different voxelized breast phantoms, selecting the glandularity, the compression and the voxel size (see Fig. 3).

The voxel size of the anthropomorphic model has been set at 0.1x0.1x0.1 mm^3. The compressor plate is included in the voxelized phantom and the compression of the breast was performed with the internal algorithm of VICTRE using FEBio [5,30,31], an open-source software focused on solving nonlinear deformation problems.

GAMOS cannot directly interpret VICTRE's output; therefore, the output file must be converted into a specific GAMOS format file that includes the material density and composition for each voxel. A Python script has been developed for this conversion, reading the encoded file generated by VICTRE and using a text file to assign the density and material for each code. The composition and density of breast tissues are based on data from a previous publication [32]. All this process can be controlled by the GUI "*Phantom Generation*" (see Fig. 1).

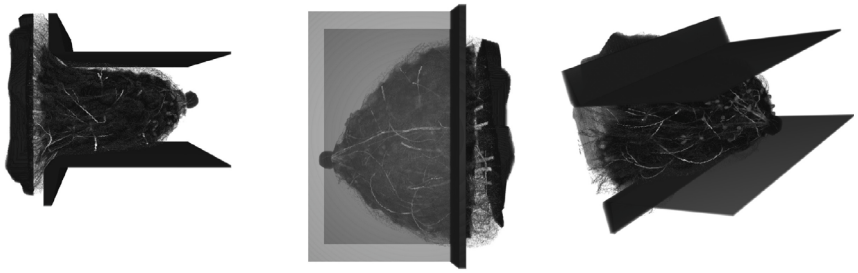

Fig. 3. 3D representation of a voxelized breast generated by VICTRE.

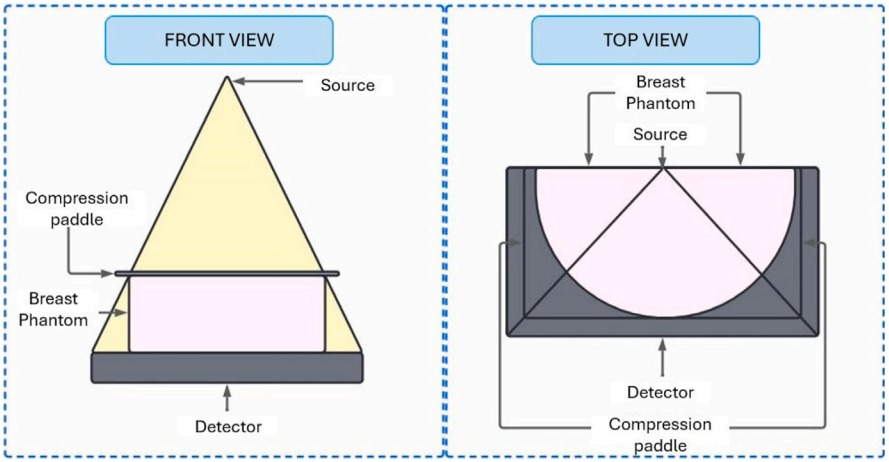

Fig. 4. Simulation setup.

Table 1
Siemens Mammomat Inspiration specifications.

Target Materials	Molybdenum and tungsten
Added filtration	30 μm molybdenum 25 μm rhodium with Mo tube 50 μm rhodium with W tube
Pixel Size	85 μm
Detector area	24 × 30 cm^2
Pixel array	2816 × 3584
Focus to image receiver (SDD)	650.0 mm (Mo target) 655.5 mm (W target)

2.2. Simulation model

Fig. 4 shows the basic geometry used for the Siemens Mammomat Inspiration system [28]. Table 1 presents the most relevant parameters of the simulated mammographic device, being selectable through the GUI. In the following sections, each part/element of the simulation model is described in detail.

2.2.1. X-ray source

The X-ray spectrum for the source was generated using the '*Spectrum Processor*' software (SPs) [33], in accordance with the guidelines of the AAPM report No 195 [29]. The emission of photons was set according to a 2D Gaussian with a sigma of 0.3 mm [13,34]. The directions of the photons follow an isotropic distribution within a right-angled pyramid whose base has the dimensions of the detector and the axis coincides with the chest wall of the patient. This configuration guarantees that all the photons generated in the source points towards the detector (see Fig. 4). This angle distribution is not available in GAMOS, so we developed and incorporated in the GAMOS workflow the necessary code to obtain the desired distribution. The implementation allows to optimize the number of events generated and therefore the time consumed by the simulation. The heel effect has not been included, following the approach of other similar modelizations [13,25].

2.2.2. Detector

Performing a comprehensive simulation that accounts for all the physical and electronic processes involved in detection is often infeasible due to its inherent complexity. Consequently, the detector response is typically approximated via suitable post-processing. Based on this premise, we have created two detector models: (1) a direct conversion detector (MCD) that focuses on the energy deposited within a uniform a-Se layer, and (2) a virtual detector (VD) that uses a scoring plane and an absorption efficiency coefficient [35–37]. Below, we describe these two approaches in detail.

- The *direct conversion detector* (MCD) includes the electromagnetic process implemented in GEANT4 via GAMOS, these are the scattering and photoelectric absorption effects as well as the fluorescence effects that take place in the detector. In this model, the energy stored in each pixel has been collected and then transformed into charge and subsequently into a signal corresponding to the pixel value of an image. A routine was developed within GAMOS to store the accumulated energy per pixel, outputting the data at the end of the simulation. This approach optimizes the simulation by reducing file writing operations and saving time.
- The *virtual detector* (VD) approach uses a scoring plane placed at the detector position to record the photon fluence. We then multiply that fluence by the absorption efficiency of the amorphous selenium [38] to estimate the energy that would be deposited in an actual detector layer. Because we do not model a full volumetric geometry for the detector, this method avoids the computational expense of tracking interactions within the detector material. Nevertheless, it still provides a reasonable approximation of the detected signal and substantially reduces simulation time.

For both models, several common considerations have been taken into account. The size of the detector varies depending on the dimensions of the phantom, thus optimizing the simulation by using the smallest possible number of events. We have defined a pixel size of 0.085 × 0.085 mm^2 and the detection area consists of a 0.2 mm thick layer of a-Se with a uniform density of 4.28 g/cm^3 and no internal microstructure [35]. This assumption preserves the main physical interactions relevant to X-ray detection without adding unnecessary computational complexity.

Additionally, the anti-scatter grid has been implemented based on the 1-D focused grid model described by G.J. Day et al. [39], which is the same approach employed by VICTRE. The grid frequency is 31 line pairs per centimeter with a grid ratio of 5. The grid was modeled with 65 μm lead strips and polystyrene as the interspace material. A binary random sampling approach was applied to determine whether the x-rays are absorbed or transmitted through the cover and the grid, as described by other authors [13]. This grid modeling approach was chosen because explicit references to its composition were not found in the manufacturer's specifications.

To optimize simulation time we made some physical assumptions:

1. It is assumed that the electrons resulting from photoelectric or Compton interactions are absorbed at the point of interaction. This is based on the premise that electrons of 30 keV have a range of less than 20 μm in water, thus eliminating the need to consider their secondary transport.
2. The possibility of blur due to electron–hole transport in the Se detector is discarded, assuming that there is no charge transfer between adjacent pixels. This is justified by the typical charge displacement in the Se detector, which is about 10 μm.[13]
3. The electron–hole pair generation gain, W+, has been considered constant at 50 eV. Despite the variability in the values of W+ and the possibility that higher values, such as 64 eV, might be required for the low energies used in mammography, this standard value is maintained [40].
4. Any fluorescence that may occur within the patient is ignored, limiting the analysis to k_α fluorescence emitted and tracked only within the Se detector.
5. Ideal beam collimators are used in the model, meaning any consideration of scatter and transmission through them is omitted.
6. The anti-scatter grid has also been modeled ideally, as described in the Section 2.2.2.

In the models created, assumptions were made due to the lack of detailed information: no patient movement during image capture, a 3D-Gaussian extended focus without off-focus radiation, and a detector with no internal semiconductor structure, assuming 100% efficiency in the fill factor. Temporal effects on the detector's response, such as persistence or ghosting, are not accounted for, although an undisclosed automatic post-processing step compensates for them. The images lack structured noise or fixed patterns, ensuring equal sensitivity in all pixels without dead pixels. Simple additive electronic noise is included without a detailed model of the readout electronics. No post-processing is performed on the images, and in the case of the anthropomorphic phantom the amount of X-rays for each breast glandularity is estimated without considering the correlation between thickness and glandularity.

2.2.3. Number of events calculation and Mean Glandular Dose (MGD)

One of the most important parameters which affect the computational time is the number of events used in the simulation. For this reason, to determine the number of events (N) in our simulations, we adopted a method similar to that followed by Badal et al. [13]. This avoids the use of variance reduction techniques, resulting in images whose pixel variance is comparable to quantum noise in real images. Additionally, this method allows for the direct estimation of the dose to the examined organ in absolute units (mGy), which is essential for accurately calculating the Mean Glandular Dose (MGD).

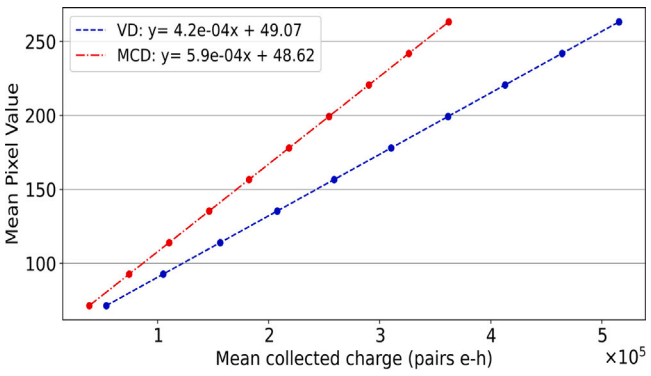

Fig. 5. Sensitivity curve for both detector models, virtual (VD) and direct conversion detector (MCD).

The air kerma provided by the SPs, expressed in $\mu Gy/mAs$, was used [33]. Concurrently, simulations were conducted to determine the kerma in a volume of air of 20x20x5 mm^3, yielding the air kerma per event ($\mu Gy/event$). This procedure ensures a direct correlation between experimental conditions and simulations.

This methodology allows us to obtain the conversion factor between (mAs/event) for a specific energy spectrum [13]. Using the tube load values (mAs) reported in the NHS report [28], we determined the number of events based on the equivalent breast thickness. The values found are in the order of 10^{11} events, varying with the thickness of the phantom. The accurate determination of the number of events that reach the detector also contributes to the precise calculation of the MGD. Determination of the Mean Glandular Dose (MGD) was achieved using the tools included in GAMOS which allows to directly measure the dose.

2.3. Image formation

The image has been generated using a Python script that takes as input the deposited energy matrix generated after the detector simulation. This code creates the image according to the following scheme:

1. The deposited energy (32-bit floating point) is converted into charge in the sensitive area of each pixel by sampling a Gaussian distribution with a mean value corresponding to the charge generated with an effective detector gain (W+) of 50 eV per detected electron–hole pair (eV) [38], and a standard deviation given by a Swank factor of 0.99 [13].
2. A randomly Poisson-distributed sample with a mean value of 5200 charges is added to each pixel value to reproduce the additive electronic noise [13].
3. A convolution is performed with a 2-D Gaussian kernel to simulate the blurring effect produced by fluorescence [41]. This kernel can be set via the user GUI.
4. A post-processing step is performed to match the simulated mean charge to the real detector's mean pixel value under equivalent entrance-dose conditions. Specifically, the mean simulated charge is compared with the mean pixel value from a raw image acquired by an actual a-Se detector (Siemens Mammomat Inspiration [28]), using a flat-field at RQA-M2 beam quality [42] (Mo/Mo, 0.032 mm Al, 28 kV, first half-value layer of 0.6 mmAl). The resulting relationship between the generated charge and the detector's pixel value is shown in Fig. 5.

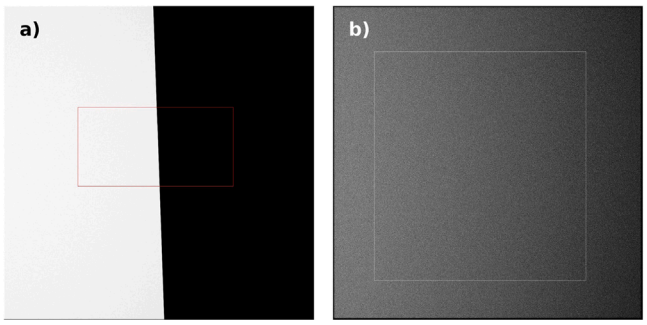

Fig. 6. Images used for performance parameter calculations. Left: edge image used to calculate the MTF. Right: flat-field image used to calculate the NNPS, showing the selected ROIs.

Table 2
EDGE phantom definition parameters (in accordance with IEC 62220-1-2:2007).

Edge material	Stainless steel ($\rho = 7.9$ g/cm^3)
Edge dimensions	120 × 60 × 0.8 mm^3
Edge modeling	GEANT-4 solid
Edge angle	2.0°

The simulation was performed on an HP Z2 Tower G9 Workstation with an Intel Core i9-13900K, 32 cores, and 128 GB of RAM, achieving a speed of $\sim 10^3$–10^4 events/s per core depending on the voxelized phantom. The use of an efficient navigation algorithm made the speed nearly independent of the phantom size [24]. Additionally, the Skip Equal Materials algorithm in GEANT4 was used to skip boundaries between contiguous voxels.

2.4. Verification and validation

Several verification processes were carried out to ensure the accuracy and reliability of our in silico model for mammography. The Validation of detector performance through the calculation of modulation transfer function (MTF), normalized noise power spectrum (NNPS), and detective quantum efficiency (DQE). The dose delivered to the tissue was verified using the AAPM TG-195 procedure. For the anthropomorphic phantom images, in addition to visual evaluation, a noise power spectrum analysis was performed for anatomical tissue ($NPS_{anatomical}$), which follows a power law.

2.4.1. MTF, NNPS and DQE

These metrics were determined in accordance with the methods described by the International Electrotechnical Commission (IEC 62220-1-2:2007 [42]), using RQA-M2 beam quality. Simulations were evaluated using both detector models and compared with reference values [28]. To ensure consistent comparisons between different systems, the normalized NPS (NNPS), derived by normalizing the NPS with the mean signal, was calculated from flat-field images using multiple regions of interest (ROIs) in homogeneous areas, while the MTF was obtained from edge images (see Fig. 6).

Table 2 shows the most relevant parameters for obtaining the edge image, always in accordance with what is described in the IEC standard [42].

The calculation of MTF and NNPS was carried out using the MAMMO QC plugin [43] for ImageJ. The Detective Quantum Efficiency (DQE) was calculated from the MTF and NNPS results, following the IEC guidelines (see Eq. (1))

$$DQE(f) = \frac{MTF(f)^2}{NNPS(f)} \times \frac{q}{N_0} \tag{1}$$

Where q is the number of electrons per absorbed photon and N_0 is the number of incident photons per unit area. The results were then compared with the specifications published by the National Health Service (NHS) [28] (see Section 3).

Table 3
Phantom's names and parameters used on the phantom generation.

Phantom name	Fat fraction	Compression thickness (mm)	Resolution (mm)
Dense	0.40	35	0.1
Heterogeneous	0.66	45	0.1
Scattered	0.85	55	0.1
Fatty	0.95	60	0.1

2.4.2. Dose verification

To validate the accuracy of x-ray transport and interaction characteristics in our Monte Carlo simulation, we followed the specifications and phantom description in TG-195 [29]. Measurement points were set at seven locations throughout the volume, including five points on the central plane parallel to the scoring plane, and two additional points directly above and below the central point, each with a volume of interest (VOI) of 4000 mm^3 (20 mm × 20 mm × 10 mm), in addition to the entire breast. For this calculation, an isotropic point source was used along with the Mo/Mo 30 kVp spectrum and monoenergetic photons at 16.8 keV. This ensures that the energy transport and deposition can be validated using the TG-195 references.

2.4.3. Anatomical noise power law

The $NPS_{anatomical}$ obtained from voxelized breast phantoms was compared to the $NPS_{anatomical}$ values for patient breast tissue from the literature [44,45].

We conducted several simulations using different voxelized realistic breast phantoms generated by VICTRE for visual assessment and evaluation of noise. The specifications of the used phantoms are detailed in Table 3. The names of the phantoms follow the BI-RADS (Breast imaging-reporting and data system) classification [46]. the generated breasts cover a wide range of patient breasts.

These images have been obtained using specific simulation parameters without undergoing the typical clinical image processing; instead, only the pixel values were adjusted by applying the sensitivity curve (see Fig. 5). This adjustment ensures that the images reflect accurate radiological densities according to the simulation's settings. The simulation area has been efficiently cropped to include only the phantom locations, optimizing CPU time and resources.

The anatomical noise power spectrum ($NPS_{anatomical}$) was obtained from these voxelized breast phantoms. The procedure to obtain this $NPS_{anatomical}$ is similar to that described above for the detector power spectrum, but in this case, it includes the presence of realistic breast tissue. A power law fit [27] (see Eq. (2)) was used to verify that the noise exhibits a structure similar to real breast images.

$$NPS_{anatomical}(f) = \alpha \cdot f^{-\beta} \tag{2}$$

3. Results

The following results highlight the verification and validation of the digital mammography system model.

3.1. NNPS, MTF and DQE

Figs. 7 and 8 show the Modulation Transfer Function (MTF) and the Normalized Noise Power Spectrum (NNPS) of the system, calculated on images obtained with the virtual detector model (VD) and with the direct conversion detector (MCD). The figures also show the values obtained from the National Health System (NHS) report [28] for the same equipment chosen in our simulation. The results of the DQE calculation are displayed in Fig. 9.

Table 4 shows the differences in MTF, NNPS, and DQE between the VD and MCD detector models and the NHS report for the spatial frequencies of 0.5 mm^{-1}, 2 mm^{-1} and 5 mm^{-1}. The modulation transfer function at 50% of its maximum value ($MTF_{50\%}$) is for VD 4.25 mm^{-1} and 4.35 mm^{-1} for MCD respectively.

Table 4
Differences between MTF, NNPS and DQE between VD and MCD models with the NHS report.

Frequency (mm^{-1})	VD differences (%)			MCD differences (%)		
	MTF	NNPS	DQE	MTF	NNPS	DQE
0.5	3.77	34.19	10.38	4.14	29.03	15.62
2.0	2.41	37.82	1.76	2.35	31.84	6.26
5.0	16.45	1.80	6.32	16.61	2.21	2.86

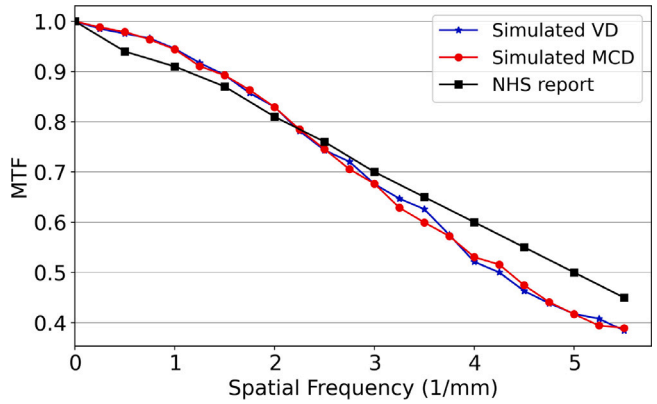

Fig. 7. Modulation Transfer Functions computed from edge image, comparison with NHS report.

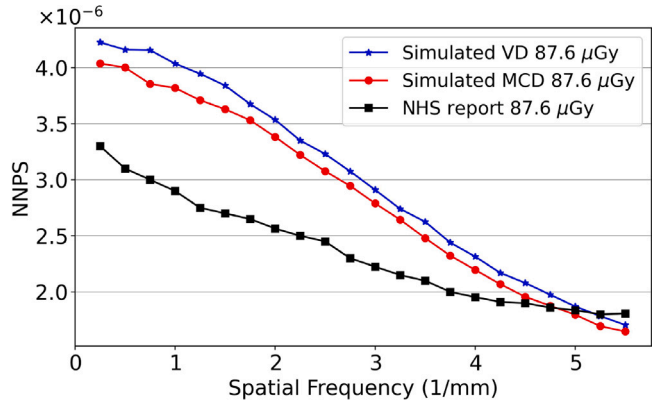

Fig. 8. Normalized Noise Power Spectrum computed from simulated flat field image, comparison with NHS report.

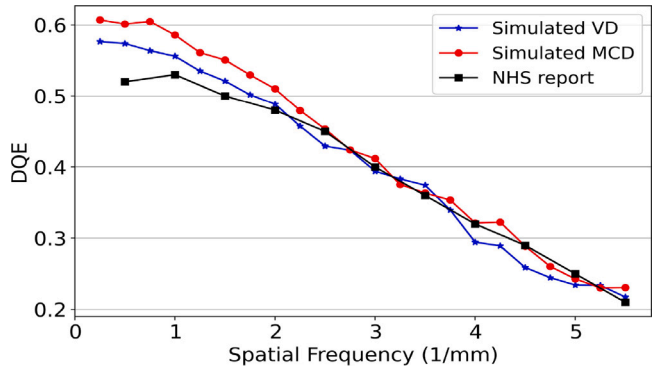

Fig. 9. Detective Quantum Efficiency (DQE) calculated using Eq. (1).

3.2. Dose verification

Energy deposited scores were compared with TG-195 reference values. Results showed (see Table 5) that simulated values closely matched with TG-195 ones, confirming the accuracy of our simulation model. The difference in energy deposition between the 16.8 keV monoenergetic and Mo/Mo spectra is slight, indicating consistent simulation across different spectral configurations.

3.3. Anatomical noise power law

Below we present the images of the phantoms, Dense, Heterogeneous, Scattered and Fatty (Fig. 10).

In Fig. 11, the radially averaged power spectrum of breast tissue noise is presented within the range [0.2–0.8] mm^{-1}. The figure also includes the NPS corresponding to the breast without anatomical structure, obtained using the TG-195 [29] phantom (green curve) and the typical values of real images [44] (shaded area), which represent the range of patient data. The parameters of the power law fit (see Eq. (2)) are shown in Table 6.

3.4. Computation time

Table 7 details the specific irradiation parameters (tube voltage and tube load) along with key simulation metrics, including the number of events and the corresponding computation times. Each event represents the complete tracking of a photon until it is absorbed, exits the system, or falls below the energy threshold. The reported simulation times were obtained using the direct conversion detector (MCD) and the breast phantoms detailed in Table 3.

Our results are consistent with those reported by di Franco et al. [25] for Geant4-based Monte Carlo simulations on CPU systems, demonstrating comparable performance under similar computational conditions.

4. Discussion

Regarding the imaging performance metrics, including MTF, NNPS, and DQE, our simulations generally align well with clinical data, though some discrepancies can be seen.

For the Modulation Transfer Function (MTF), the differences observed can be attributed to the simplified modeling of the detector, particularly the lack of detailed processes such as electron–hole transport and secondary electron tracking. This simplification can artificially enhance the spatial resolution in simulations, leading to a higher MTF compared to real clinical measurements, as highlighted by Sarno et al. [47]. The absence of these internal interactions results in a reduced blurring effect, which does not fully capture the intrinsic energy spread within the detector material.

As shown in Fig. 8, discrepancies in the NNPS values between the VD and MCD models are evident when compared to published results. These discrepancies may be attributed to the blurring process incorporated in the image simulation. This blurring process is intended to replicate the effects of fluorescence emission (VD) and electron cross-talk (VD y MCD) within the detector signal, and it has the potential to modify the noise characteristics of the image.

Although the MCD model provides a more detailed representation of physical processes — such as energy deposition and fluorescence emission — compared to the VD model, the observed lower NNPS for MCD model is unexpected and requires further investigation.

Lastly, for the Detective Quantum Efficiency (DQE), while our results show a general consistency with clinical data, the limitations identified in the MTF and NNPS directly impact DQE calculations. Despite these challenges, the overall reliability of the simulated DQE highlights the validity of our model as a tool for virtual clinical trials.

Table 5
Energy absorbed per initial photon, both in the simulation and that reported in TG-195 and their differences. VOIs are located as shown in Fig. 2.

Point evaluated	Flat field (16.8 keV)			Flat field (30 kVp Mo-Mo)		
	E_{abs}^{sim} (eV)	E_{abs}^{TG-195} (eV)	diff. (%)	E_{abs}^{sim} (eV)	E_{abs}^{TG-195} (eV)	diff. (%)
Breast tissue	4685.5 ± 0.2	4700.46 ± 0.08	−0.32	4288.4 ± 0.2	4296.79 ± 0.07	−0.19
VOI 1	17.71 ± 0.02	17.782 ± 0.005	−0.41	16.48 ± 0.02	16.53 ± 0.005	−0.21
VOI 2	17.92 ± 0.02	17.993 ± 0.005	−0.43	16.61 ± 0.02	16.67 ± 0.005	−0.37
VOI 3	18.01 ± 0.02	18.074 ± 0.005	−0.36	16.77 ± 0.02	16.81 ± 0.005	−0.25
VOI 4	17.41 ± 0.02	17.550 ± 0.005	−0.80	16.21 ± 0.02	16.26 ± 0.005	−0.34
VOI 5	17.71 ± 0.02	17.787 ± 0.005	−0.44	16.47 ± 0.02	16.53 ± 0.005	−0.34
VOI 6	5.51 ± 0.01	5.573 ± 0.003	−1.08	6.00 ± 0.01	6.049 ± 0.004	−0.86
VOI 7	56.33 ± 0.04	56.29 ± 0.01	0.07	50.20 ± 0.03	50.07 ± 0.01	0.24

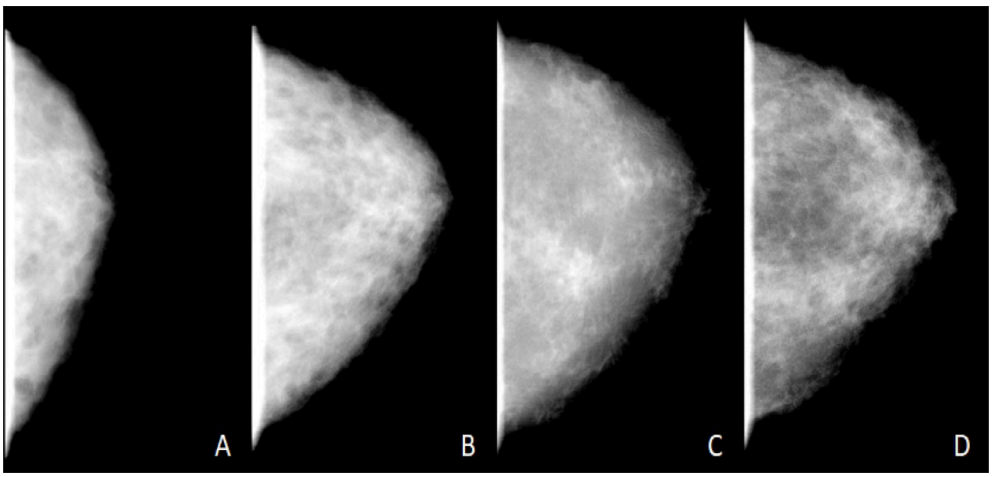

Fig. 10. Simulated images of the breast phantom. A.- Dense phantom, B.- Heterogeneous phantom, C.- Fatty phantom and D.- Scattered phantom.

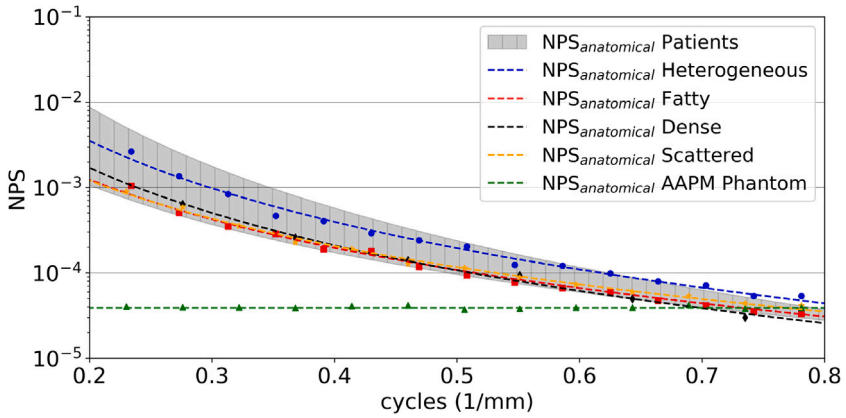

Fig. 11. Radially averaged power spectrum of anatomical noise (0.2–0.8 mm^2). The curves represent the NPS$_{anatomical}$ for the Dense, Heterogeneous, Scattered and Fatty breast models from Table 3. The shaded area indicates patient data from [45], based on parameters from Table 3. The green curve shows the flat NPS of the unstructured TG195 phantom. (For interpretation of the references to color in this figure legend, the reader is referred to the web version of this article.)

Table 6
Parameters of the NPS power-law fit.

Phantom name	β	α [mm^2]	R^2
Dense	3.027	1.312×10^{-5}	0.9980
Heterogeneous	3.165	2.173×10^{-5}	0.9615
Scattered	2.554	1.989×10^{-5}	0.9917
Fatty	2.773	1.534×10^{-5}	0.9600

Future work should focus on refining these aspects, for example, a different electronic noise modeling, as proposed by Sengupta et al. [41], or incorporating more sophisticated models of scatter reduction to achieve closer alignment with experimental data [13,34].

Validation against the AAPM Task Group 195 (TG-195) reference values has confirmed the accuracy of our simulation methods, specifically in dose calculations. The successful alignment of our simulated dose results with established benchmarks illustrates the potential of our simulation framework for conducting virtual clinical trials and advancing diagnostic imaging research in mammography. The good agreement observed in the dose comparison further reinforces the validity of our model. These validations, alongside the observed discrepancies, highlight areas for improvement while reinforcing the overall robustness of the simulation framework.

The comparison of the anatomical noise power law highlights two key findings: first, for the breast model without tissue structure, the noise appears flat, indicating the absence of the complex anatomical structure; second, the power law fit values, specifically the exponent

Table 7
Irradiation parameters for simulations using VD and breast phantoms (Table 3), using 25 cores.

Phantom name (type)	Events/(s· core)	N_{events}	$t_{simulation}$ (s)	Tube load (mAs)	Tube voltage (kVp)	MGD (mGy)
Dense	$1.1 \cdot 10^4$	$1.879 \cdot 10^{11}$	$7.21 \cdot 10^5$	51.62	28	0.65
Heterogeneous	$1.5 \cdot 10^4$	$2.392 \cdot 10^{11}$	$6.38 \cdot 10^5$	65.68	28	0.82
Scattered	$1.4 \cdot 10^4$	$3.464 \cdot 10^{11}$	$9.90 \cdot 10^5$	95.65	30	1.22
Fatty	$1.5 \cdot 10^4$	$3.433 \cdot 10^{11}$	$9.15 \cdot 10^5$	94.29	30	1.14

β, are similar to those observed in patient data, demonstrating that the noise properties of the structured breast models in our simulations closely resemble those of real breast tissue [44,45].

The computation times reported in our study align with those described by di Franco et al. [25] for CPU-based Monte Carlo simulations, demonstrating comparable performance in terms of event rates under similar computational conditions. However, several key advancements in our work enhance both the precision and efficiency of the simulations. First, we employ a higher resolution for the breast phantom (0.1 mm) compared to the $[0.194, 0.427]mm$ used by di Franco, enabling more detailed anatomical modeling. Additionally, our simulations incorporate a realistic direct conversion detector (MCD), which takes into account most relevant electromagnetic processes, including scattering, photoelectric absorption, and fluorescence effects within the detector material.

The simulated images of the breast phantoms, as presented in Fig. 10, demonstrate the efficacy of our simulation approach in reproducing detailed anatomical features across diverse breast compositions (Dense, Heterogeneous, Scattered and Fatty). The high-resolution images capture subtle variations in tissue density and structure, which are essential for realistic testing of mammographic procedures and equipment. This capability is particularly important for virtual clinical trials where diverse anatomical representations are necessary to evaluate the performance of imaging systems under varied clinical conditions.

The clarity and accuracy of these phantom images not only validate our simulation parameters and computational techniques but also highlight the potential of our model to serve as a tool for enhancing the understanding of mammographic imaging. By providing a controlled environment to test and optimize imaging parameters, these simulations can help in refining diagnostic strategies and potentially lead to improvements in early breast cancer detection.

Furthermore, the consistent quality across images of different phantom types supports the robustness of our simulation framework, affirming its reliability for extended applications in breast imaging research and development. This demonstrates our model's ability to handle variable anatomical complexities, making it a versatile tool in the advancement of mammographic technology.

The use of GAMOS [24] provided an accessible and modular framework for the simulation of a mammography system. Adapting GAMOS for this purpose facilitates an efficient implementation of the simulation and opens possibilities for future improvements, such as enhanced modeling of the anti-scatter grid, more realistic simulation of the detector response and the physical processes involved in Phase Contrast Imaging.

While our simulation framework offers significant advantages in terms of flexibility and comprehensive physical modeling, it is acknowledged that the computational time required is greater than that of specialized GPU-based codes specifically designed for mammographic image simulation. This trade-off stems from the versatility provided by GEANT4 and the user-friendly interface of GAMOS, which allow for the inclusion of complex geometries and user-defined physics effects without extensive programming. The ability to easily modify and extend the model makes our framework a valuable tool for detailed and customizable mammographic imaging studies—particularly when exploring new detector designs [48], phase-contrast imaging (PCI) [20], or emerging spectral mammography techniques [49]. We acknowledge that further optimization of the simulation times would be beneficial and plan to address this in future work.

Furthermore, our simulation framework is designed to be highly adaptable to various state-of-the-art detector models without requiring modifications to the core simulation code. This is because the simulation is designed to manage the energy deposition process, obtaining the photon fluence at the detector's entrance. To incorporate a different detector model, one has simply to modify the geometry, the physics process (or include new ones), and the material using GAMOS scripts or our GUI. After the detector simulation, the post-processing tools developed for energy deposition are applied to generate the mammographic image. This modular approach allows for the seamless integration of new detector technologies, ensuring that our framework can remain up-to-date with advancements in detector design and functionality without necessitating significant alterations to the existing simulation infrastructure.

5. Conclusions

This study presents a simulation using the GAMOS framework with GEANT4, demonstrating reasonable accuracy in simulating the selected detector model. Notably, this is the first time GAMOS has been used to produce an X-ray image. The results for the Modulation Transfer Function (MTF), Normalized Noise Power Spectrum (NNPS), and Detective Quantum Efficiency (DQE) are comparable to those reported in the published literature, while dose calculations validated against the AAPM TG-195 report further confirm the model's reliability.

Future modifications of the code could include a better modeling of the anti-scatter grid and a more realistic simulation of the detection processes. These improvements could potentially increase the accuracy of the simulation results and bring them even closer to actual measurements.

CRediT authorship contribution statement

F.R. Lozano: Conceptualization, Formal analysis, Methodology, Resources, Software, Validation, Visualization, Writing – original draft. **V. Sanchez-Lara:** Conceptualization, Formal analysis, Methodology, Resources, Software, Validation, Visualization, Writing – original draft. **C. Huerga:** Conceptualization, Formal analysis, Methodology, Supervision, Validation, Writing – review & editing. **Luis C. Martinez-Gomez:** Conceptualization, Methodology, Resources, Supervision, Validation, Writing – review & editing. **D. Garcia-Pinto:** Conceptualization, Methodology, Resources, Project administration, Supervision, Validation, Writing – review & editing.

Funding

This work was supported by the Ministry of Science and Innovation of Spain. This work forms part of the subproject of VICTORIA project: Pre-clinical experiments for developing and optimizing new Imaging in Breast Cancer, Ref: PID2021-123390OB-C22, funded by MCIN/AEI/10.13039/501100011033.

Declaration of competing interest

The authors declare the following financial interests which may be considered as potential competing interests: financial support was provided by the Ministry of Science and Innovation of Spain.

References

[1] Marshall NW, Bosmans H. Performance evaluation of digital breast tomosynthesis systems: comparison of current virtual clinical trial methods. Phys Med Biol 2022;67(22). http://dx.doi.org/10.1088/1361-6560/ac9a34.

[2] Hadjipanteli A, Elangovan P, Mackenzie A, Looney PT, Wells K, Dance DR, et al. The effect of system geometry and dose on the threshold detectable calcification diameter in 2D-mammography and digital breast tomosynthesis. Phys Med Biol 2017;62(3):858–77. http://dx.doi.org/10.1088/1361-6560/aa4f6e.

[3] Abadi E, Segars WP, Tsui BMW, Kinahan PE, Bottenus N, Frangi AF, et al. Virtual clinical trials in medical imaging: a review. J Med Imaging 2020;7(4):042805. http://dx.doi.org/10.1117/1.JMI.7.4.042805, URL https://www.ncbi.nlm.nih.gov/pmc/articles/PMC7148435/.

[4] Wang J, Liu Y, Hu A, Wu Z, Zhang H, Li J, et al. THUBreast: an open-source breast phantom generation software for x-ray imaging and dosimetry. Phys Med Biol 2024;69(6). http://dx.doi.org/10.1088/1361-6560/ad2881.

[5] Graff CG. A new, open-source, multi-modality digital breast phantom. In: Kontos D, Flohr TG, editors. In: Medical imaging 2016: physics of medical imaging, vol. 9783, SPIE, International Society for Optics and Photonics; 2016, 978309. http://dx.doi.org/10.1117/12.2216312.

[6] Badano A, Graff CG, Badal A, Sharma D, Zeng R, Samuelson FW, et al. Evaluation of digital breast tomosynthesis as replacement of full-field digital mammography using an in silico imaging trial. JAMA Netw Open 2018;1(7):e185474. http://dx.doi.org/10.1001/jamanetworkopen.2018.5474.

[7] Massera RT, Bosmans H, Rodriguez Perez S, Marshall N. A combined analytical and Monte Carlo method for detailed simulations of antiscatter grids in x-ray medical imaging: implementing scatter within the grid. Phys Med Biol 2024;69(7):0–16. http://dx.doi.org/10.1088/1361-6560/ad2b93.

[8] Golosio B, Schoonjans T, Brunetti A, Oliva P, Masala GL. Monte Carlo simulation of X-ray imaging and spectroscopy experiments using quadric geometry and variance reduction techniques. Comput Phys Comm 2014;185(3):1044–52. http://dx.doi.org/10.1016/j.cpc.2013.10.034, URL http://dx.doi.org/10.1016/j.cpc.2013.10.034.

[9] Bliznakova K, Kolitsi Z, Pallikarakis N. Dual-energy mammography: Simulation studies. Phys Med Biol 2006;51(18):4497–515. http://dx.doi.org/10.1088/0031-9155/51/18/004.

[10] Delis H, Spyrou G, Panayiotakis G, Tzanakos G. DOSIS: A Monte Carlo simulation program for dose related studies in mammography. Eur J Radiol 2005;54(3):371–6. http://dx.doi.org/10.1016/j.ejrad.2004.07.014.

[11] Sarno A, Mettivier G, Russo P. Air kerma calculation in Monte Carlo simulations for deriving normalized glandular dose coefficients in mammography. Phys Med Biol 2017;62(14):N337–49. http://dx.doi.org/10.1088/1361-6560/aa7016.

[12] Badal A, Badano A. Accelerating Monte Carlo simulations of photon transport in a voxelized geometry using a massively parallel graphics processing unit. Med Phys 2009;36:4878–80. http://dx.doi.org/10.1118/1.3231824.

[13] Badal A, Sharma D, Graff C, Zeng R, Badano A. Mammography and breast tomosynthesis simulator for virtual clinical trials. Comput Phys Comm 2020;261:107779. http://dx.doi.org/10.1016/j.cpc.2020.107779.

[14] Mettivier G, Sarno A, Lai Y, Golosio B, Fanti V, Italiano ME, et al. Virtual clinical trials in 2D and 3D X-ray breast imaging and dosimetry: Comparison of CPU-based and GPU-based Monte Carlo codes. Cancers 2022;14(4). http://dx.doi.org/10.3390/cancers14041027, URL https://www.mdpi.com/2072-6694/14/4/1027.

[15] Ghetti C, Ortenzia O, Pagan L, Golinelli P, Nitrosi A, Sghedoni R, et al. Physical and dosimetric characterisation of different contrast-enhanced digital mammographic systems: A multicentric study. Phys Medica: Eur J Med Phys 2024;120. http://dx.doi.org/10.1016/j.ejmp.2024.103334.

[16] Lewis RA. Medical phase contrast x-ray imaging: current status and future prospects. Phys Med Biol 2004;49(16):3573–83. http://dx.doi.org/10.1088/0031-9155/49/16/005.

[17] Wu X, Liu H. Phase-space formulation for phase-contrast x-ray imaging. Appl Opt 2005;44(28):5847–54. http://dx.doi.org/10.1364/ao.44.005847.

[18] Agostinelli S, Allison J, Amako K, Apostolakis J, Araujo H, Arce P, et al. Geant4—a simulation toolkit. Nucl Instruments Methods Phys Res Sect A: Accel Spectrometers, Detect Assoc Equip 2003;506(3):250–303. http://dx.doi.org/10.1016/S0168-9002(03)01368-8, URL https://www.sciencedirect.com/science/article/pii/S0168900203013688.

[19] Wang Z, Huang Z, Zhang L, Chen Z, Kang K. Implement X-ray refraction effect in Geant4 for phase contrast imaging. IEEE Nucl Sci Symp Conf Rec 2009;2395–8. http://dx.doi.org/10.1109/NSSMIC.2009.5402180.

[20] Langer M, Cen Z, Rit S, Létang JM. Towards Monte Carlo simulation of X-ray phase contrast using GATE. Opt Express 2020;28(10):14522. http://dx.doi.org/10.1364/oe.391471.

[21] Brombal L, Rigon L, Arfelli F, Menk RH, Brun F. A Geant4 tool for edge-illumination X-ray phase-contrast imaging. J Instrum 2022;17(1). http://dx.doi.org/10.1088/1748-0221/17/01/C01043.

[22] Tavakoli Taba S, Baran P, Nesterets YI, Pacile S, Wienbeck S, Dullin C, et al. Comparison of propagation-based CT using synchrotron radiation and conventional cone-beam CT for breast imaging. Eur Radiol 2020;30(5):2740–50. http://dx.doi.org/10.1007/s00330-019-06567-0.

[23] Gassert FT, Urban T, Frank M, Willer K, Noichl W, Buchberger P, et al. X-ray dark-field chest imaging: Qualitative and quantitative results in healthy humans. Radiology 2021;301(2):389–95. http://dx.doi.org/10.1148/radiol.2021210963.

[24] Arce P, Ignacio Lagares J, Harkness L, Pérez-Astudillo D, Cañadas M, et al. Gamos: A framework to do Geant4 simulations in different physics fields with an user-friendly interface. Nucl Instruments Methods Phys Res Sect A: Accel Spectrometers, Detect Assoc Equip 2014;735:304–13. http://dx.doi.org/10.1016/j.nima.2013.09.036, URL https://www.sciencedirect.com/science/article/pii/S0168900213012709.

[25] di Franco F, Sarno A, Mettivier G, Hernandez AM, Bliznakova K, Boone JM, et al. GEANT4 Monte Carlo simulations for virtual clinical trials in breast X-ray imaging: Proof of concept. Phys Medica 2020;74(November 2019):133–42. http://dx.doi.org/10.1016/j.ejmp.2020.05.007.

[26] Chen L, Abbey CK, Boone JM. Association between power law coefficients of the anatomical noise power spectrum and lesion detectability in breast imaging modalities. Phys Med Biol 2013;58(6):1663. http://dx.doi.org/10.1088/0031-9155/58/6/1663.

[27] Burgess AE, Jacobson FL, Judy PF. Human observer detection experiments with mammograms and power-law noise. Med Phys 2001;28(4):419–37. http://dx.doi.org/10.1118/1.1355308, arXiv:https://aapm.onlinelibrary.wiley.com/doi/pdf/10.1118/1.1355308 URL https://aapm.onlinelibrary.wiley.com/doi/abs/10.1118/1.1355308.

[28] Strudley CJ, Warren LM, Young KC. Technical evaluation of the Siemens mammomat inspiration digital breast tomosynthesis system. Tech. rep. NHSBSP Equipment Report 1306, version 2, 2015.

[29] Sechopoulos I, Ali ESM, Badal A, Badano A, Boone JM, Kyprianou IS, et al. Monte Carlo reference data sets for imaging research: Executive summary of the report of AAPM research committee task group 195. Med Phys 2015;42(10):5679–91. http://dx.doi.org/10.1118/1.4928676, arXiv:https://aapm.onlinelibrary.wiley.com/doi/pdf/10.1118/1.4928676 URL https://aapm.onlinelibrary.wiley.com/doi/abs/10.1118/1.4928676.

[30] Maas SA, Ellis BJ, Ateshian GA, Weiss JA. FEBio: Finite elements for biomechanics. J Biomech Eng 2012;134(1):011005. http://dx.doi.org/10.1115/1.4005694, arXiv:https://asmedigitalcollection.asme.org/biomechanical/article-pdf/134/1/011005/5665064/011005_1.pdf.

[31] Puso MA, Weiss JA. Finite element implementation of anisotropic quasi-linear viscoelasticity using a discrete spectrum approximation. J Biomech Eng 1998;120(1):62–70. http://dx.doi.org/10.1115/1.2834308, arXiv:https://asmedigitalcollection.asme.org/biomechanical/article-pdf/120/1/62/5666098/62_1.pdf.

[32] Woodard HQ, White DR. The composition of body tissues. Br J Radiol 1986;59(708):1209–18. http://dx.doi.org/10.1259/0007-1285-59-708-1209, arXiv:https://academic.oup.com/bjr/article-pdf/59/708/1209/54336820/0007-1285-59-708-1209.pdf.

[33] Cranley K, Gilmore BJ, Fogarty GWA, Deponds L. Catalogue of diagnostic x-ray spectra and other data. J Radiol Prot 1997;18:026. http://dx.doi.org/10.1088/0952-4746/18/1/026, IPEM Report No. 78.

[34] Sarno A, Tucciariello RM. Simulated sensor characterization for virtual clinical trials in mammography and digital breast tomosynthesis. J Instrum 2022;17(01):C01041. http://dx.doi.org/10.1088/1748-0221/17/01/C01041.

[35] Kasap S, Frey JB, Belev G, Tousignant O, Mani H, Greenspan J, Laperriere L, Bubon O, Reznik A, DeCrescenzo G, Karim KS, Rowlands JA. Amorphous and polycrystalline photoconductors for direct conversion flat panel X-Ray image sensors. Sensors 2011;11(5):5112–57. http://dx.doi.org/10.3390/s110505112, URL https://www.mdpi.com/1424-8220/11/5/5112.

[36] Zhao W, Ji W, Debrie A, Rowlands J. Imaging performance of amorphous selenium based flat-panel detectors for digital mammography: Characterization of a small area prototype detector. Med Phys 2003;30:254–63. http://dx.doi.org/10.1118/1.1538233.

[37] Zhou J, Zhao B, Zhao W. SU-FF-I-39: A computer simulation platform for the optimization of breast tomosynthesis system. Med Phys 2005;32(6Part3). http://dx.doi.org/10.1118/1.1997519, 1912–1912 URL https://aapm.onlinelibrary.wiley.com/doi/abs/10.1118/1.1997519.

[38] Stone MF, Zhao W, Jacak BV, O'Connor P, Yu B, Rehak P. The x-ray sensitivity of amorphous selenium for mammography. Med Phys 2002;29(3):319–24. http://dx.doi.org/10.1118/1.1449874, arXiv:https://aapm.onlinelibrary.wiley.com/doi/pdf/10.1118/1.1449874 URL https://aapm.onlinelibrary.wiley.com/doi/abs/10.1118/1.1449874.

[39] Day GJ, Dance DR. X-ray transmission formula for antiscatter grids. Phys Med Biol 1983;28(12):1429. http://dx.doi.org/10.1088/0031-9155/28/12/008.

[40] Fang Y, Karim KS, Badano A. Effect of burst and recombination models for Monte Carlo transport of interacting carriers in a-Se x-ray detectors on Swank noise. Med Phys 2014;41(1):011904. http://dx.doi.org/10.1118/1.4842435, arXiv:https://aapm.onlinelibrary.wiley.com/doi/pdf/10.1118/1.4842435 URL https://aapm.onlinelibrary.wiley.com/doi/abs/10.1118/1.4842435.

[41] Sengupta A, Badal A, Makeev A, Badano A. Computational models of direct and indirect X-ray breast imaging detectors for in silico trials. Med Phys 2022;49(11):6856–70. http://dx.doi.org/10.1002/mp.15935, arXiv:https://aapm.onlinelibrary.wiley.com/doi/pdf/10.1002/mp.15935 URL https://aapm.onlinelibrary.wiley.com/doi/abs/10.1002/mp.15935.

[42] IEC 62220-1-2. Medical electrical equipment – Characteristics of digital X-ray imaging devices – Part 1-2: Determination of the detective quantum efficiency – Detectors used in mammography.

[43] Porzio M, Konstantinidis AC. MamMO_QC: Free software for quality control (QC) analysis in digital mammography and digital breast tomosynthesis compliant with the European guidelines and EUREF/EFOMP protocols. Biomed Phys Eng Express 2021;7(6). http://dx.doi.org/10.1088/2057-1976/ac2076.

[44] Reiser I, Edwards A, Nishikawa RM. Validation of a power-law noise model for simulating small-scale breast tissue. Phys Med Biol 2013;58:6011–27. http://dx.doi.org/10.1088/0031-9155/58/17/6011.

[45] Cockmartin L, Bosmans H, Marshall NW. Comparative power law analysis of structured breast phantom and patient images in digital mammography and breast tomosynthesis. Med Phys 2013;40(8):081920. http://dx.doi.org/10.1118/1.4816309, arXiv:https://aapm.onlinelibrary.wiley.com/doi/pdf/10.1118/1.4816309 URL https://aapm.onlinelibrary.wiley.com/doi/abs/10.1118/1.4816309.

[46] American College of Radiology BI-RADS Committee. Atlas, breast imaging reporting and data system. 5th ed. Reston VA: American College of Radiology; 2013.

[47] Sarno A, Tucciariello RM, Fantacci ME, Traino AC, Valero C, Stasi M. A model for a linear a-se detector in simulated X-Ray breast imaging with Monte Carlo software. IEEE Trans Radiat Plasma Med Sci 2024;8(3):263–8. http://dx.doi.org/10.1109/TRPMS.2024.3349563.

[48] Breemen A, Simon M, Tousignant O, Shanmugam S, Steen J-L, Akkerman H, et al. Curved digital X-ray detectors. Npj Flex Electron 2020;4:22. http://dx.doi.org/10.1038/s41528-020-00084-7.

[49] James J, Tennant S. Contrast-enhanced spectral mammography (CESM). Clin Radiol 2018;73(8):715–23. http://dx.doi.org/10.1016/j.crad.2018.05.005, URL https://www.sciencedirect.com/science/article/pii/S000992601830182X.